Applications of Wavelet Analysis in Differential Propagation Phase Shift Data De-noising

HU Zhiqun* and LIU Liping

State Key Laboratory of Severe Weather, Chinese Academy of Meteorological Sciences, Beijing 100081

ABSTRACT

Using numerical simulation data of the forward differential propagation shift (Φ_{DP}) of polarimetric radar, the principle and performing steps of noise reduction by wavelet analysis are introduced in detail. Profiting from the multiscale analysis, various types of noises can be identified according to their characteristics in different scales, and suppressed in different resolutions by a penalty threshold strategy through which a fixed threshold value is applied, a default threshold strategy through which the threshold value is determined by the noise intensity, or a Φ_{DP} penalty threshold strategy through which a special value is designed for Φ_{DP} de-noising. Then, a hard- or soft-threshold function, depending on the de-noising purpose, is selected to reconstruct the signal. Combining the three noise suppression strategies and the two signal reconstruction functions, and without loss of generality, two schemes are presented to verify the de-noising effect by dbN wavelets: (1) the penalty threshold strategy with the soft threshold function scheme (PSS); (2) the Φ_{DP} penalty threshold strategy with the soft threshold function scheme (PPSS). Furthermore, the wavelet de-noising is compared with the mean, median, Kalman, and finite impulse response (FIR) methods with simulation data and two actual cases. The results suggest that both of the two schemes perform well, especially when Φ_{DP} data are simultaneously polluted by various scales and types of noises. A slight difference is that the PSS method can retain more detail, and the PPSS can smooth the signal more successfully.

Key words: polarimetric radar, wavelet analysis, differential propagation phase shift, de-noising

1. Introduction

Dual polarimetric weather radars will be widely used in the coming years. One of the reasons is that these radars are able to obtain the specific differential phase (K_{DP}). K_{DP} is defined as the slope of the range profiles of the differential propagation phase shift (Φ_{DP}) between the horizontal (H) and vertical (V) polarization states (Seliga and Bringi, 1978; Jameson, 1985; Bringi and Chandrasekar, 2001), and it is immune to rain attenuation, partial blockage and radar calibration Besides, K_{DP} has a nearly linear relationship with the rain intensity, even in the presence of hail (Aydin et al., 1995; Zrnić and Ryzhkov, 1996; Chandrasekar et al., 2008). For example, the coefficient β in the empirical formula

$$R_{DP} = \alpha K_{DP}^{\beta}$$

for rainfall R_{DP} estimation by K_{DP} is given as 0.9056, and α as 44.806, 23.918 and 15.060 in S-, C- and X-band radars, respectively (Zhang et al., 2001). These properties make K_{DP} act as one of the important parameters of dual polarimetric weather radar. The value of Φ_{DP} is the difference between the horizontal- and vertical-direction phases, and its magnitude is one order of magnitude lower than the phase obtained from only one direction. As a result, Φ_{DP} is more easily affected by system noise, random fluctuation, and ground clutters, and hereinafter all non-real Φ_{DP} are collectively referred to as noises that need to be identified and de-noised. In particular, in a small signal-to-noise ratio (SNR), Φ_{DP} is always noisy and unstable (Hu et al., 2012). Besides, the actual radial profile of the total differential phase (Ψ_{DP}) contains both Φ_{DP} and the differential backscatter phase shift (δ). Therefore, how to reduce the Φ_{DP} noise is crucial for polarimetric radar applications, which need not only effectively suppress all kinds of noises and δ, but also maintain the cloud and precipitation information as much as possible.

In general, there are two considerations in de-noising, i.e., smoothness and similarity, and they are performed differently in the time and frequency domains. For instance, using a median or mean filter in the time domain, the signal is more likely to reflect the similarity rather than the smoothness. On the other hand, using a Fourier transform in the frequency domain, it is easy to make the signal infinitely smooth by filtering out the high frequency noise, but some informative signals are inevitably filtered out for their small energy. For dual polarimetric radar, it is usually the indications of the loca-

* Corresponding author: HU Zhiqun
  Email: huzq@cams.cma.gov.cn

tion of clutter and large reflectivity gradient that causes Φ_{DP} to oscillate rapidly in several gates, which are important in the clutter identification, and echo track algorithm, so they should not be filtered out initially before the relevant tasks have been finished.

The traditional techniques of noise reduction include range filtering, linear fitting, and a combination of the two. An iterative filtering technique separating δ from the propagation phase has been presented (Hubbert et al., 1993; Hubbert and Bringi, 1995). Wang and Chandrasekar (2009) presented an algorithm to unwrap phase wrapping and keep the spatial gradients of rainfall for high-resolution K_{DP}. He et al. (2009) introduced the Kalman filter method to separate Φ_{DP} and δ components, and filter out the random noises. Hu et al. (2012) combined the Φ_{DP} standard deviation with the horizontal and vertical cross- correlation coefficient (ρ_{HV}) to verify the valid Φ_{DP} value, and then smoothed Φ_{DP} using data collected in field experiments.

Owing to the advantage of multiscale analysis, wavelet analysis has recently become popular as a de-noising method. The history of wavelets can be traced back to Harr's work in 1909. However, from the modern viewpoint, wavelet analysis was not practicable until Caldero introduced a prototype in 1960, and the technique was not improved for 20 years until the work of Grossmann and Morlet (1984). Wavelets were widely used after 1986 because of the foundation developed by Meyer (1993), Mallat (1989, 1992), Daubechies (1988), and other scientists. Subsequently, wavelet analysis has rapidly developed and become an emerging subject that is arguably the most significant achievement in signal processing since Fourier analysis (Yang, 2007).

Wavelet analysis can localize a signal in both the time and frequency domain, and enables one to perform multiscale analysis to extract information effectively by means of signal zoom and translation. The signal information is not lost during the processes, only a new equivalent representation. Because the generating wavelet function is very flexible a suitable generating wavelet function can be selected to enlarge and extract the interesting information from part of the signal, and lessen or keep the others for further analysis. Utilizing the multiresolution characteristic, the wavelet coefficients in different scales can be verified as to whether they represent useful information or meaningless noise by a certain threshold. Wavelet-based noise reduction, especially the threshold strategy, is currently a very active field, and has become the most popular de-noising method for its simplicity and effectiveness. Mallat and Hwang (1992) proposed a signal and image multiscale edge representation technique according to the signal singularity, and introduced a filtering method of maximum module reconstruction based on the mathematical description of the Lipschitz exponent on the multiscale signal, image and noise characteristics. Utilizing the signal correlation among the scales, Xu et al. (1994) proposed a spatially selective noise filtration (SSNF) algorithm. Donoho (1995) presented the soft and hard threshold functions during the signal reconstruction. In recent years, many new threshold strategies and functions have been proposed, which have

greatly enriched the technique of wavelet de-noising.

However, the application of wavelet analysis in weather radar is rare, except for the occasional use in radar image recognition and processing. Jordan et al. (1997) developed an algorithm using wavelets to filter the ground clutters and noises in wind profile radar. A wavelet-based approach that can improve the capability in mesocyclone discrimination was reported by Desrochers and Yee (1999). Liu et al. (2007) developed a wavelet-based algorithm to detect tornadoes from Doppler weather radar radial velocity. Despite these applications, wavelet analysis is still rarely used in polarimetric radar de-noising.

In the second section of this paper, the principles of wavelet noise reduction are introduced in detail, wherein a Φ_{DP} penalty threshold strategy is addressed according to its characteristic. In the third section, the de-noising process is described by means of a simulated radar beam that passes through two rain cells of different size, and the Φ_{DP} is interposed in the fluctuation in several gates to verify the ability of identifying clutter, added some degrees in a short and a long gates (distance) to contrast the de-noising effect to different scales δ noises. Furthermore, a white noise of SNR 15dB is mixed into Φ_{DP} to demonstrate the suppression to thermal noise, respectively In the fourth section, the de-noising effects with wavelet analysis are contrasted with mean, median, finite impulse response (FIR, Hubbert and Bringi, 1995), and Kalman filters via two actual observational cases. Finally, a summary and discussion of wavelet de-noising are presented in the last section.

2. Wavelet analysis

The steps of wavelet de-noising are: an appropriate wavelet function is selected to deconstruct a signal into multiresolution signals; the detail coefficients (from the high-pass filter) that generally represent noises are suppressed by a threshold strategy; and then the signal is reconstructed with a threshold function.

2.1. *Wavelet functions*

Similar to a Fourier transform, if a set of functions that is formed by a function that can be zoomed and translated to constitute dense orthogonal bases, then a signal with finite energy can be deconstructed into the bases. So, the signal is separated into signals with different resolutions, and the interesting parts in the signal can be observed in each resolution. This type of function, which requires a compact support set, i.e., quickly decays to zero in a limited region, is known as the generating wavelet. The set of orthogonal bases formed by the generating wavelet is defined as the wavelet function.

Definition: if $\psi(t) \in L^2(\boldsymbol{R})$ and $\hat{\psi}(0) = 0$, the functions $\{\psi_{a,b}(t)\}$

$$\psi_{a,b}(t) = |a|^{1/2} \psi\left(\frac{t-b}{a}\right), \quad b \in \boldsymbol{R}, \quad a \in \boldsymbol{R} - \{0\} \quad (1)$$

is called a continuous wavelet, where $\psi(t)$ is the basic

wavelet or generating wavelet in function space $L^2(\boldsymbol{R})$, t is the variable in real number field $\boldsymbol{R}$, a is the scale or striction coefficient b is the translation factor, and satisfies the admissible condition

$$C_\psi = \int_{-\infty}^{\infty} \frac{|\hat{\psi}(\omega)|^2}{\omega} d\omega < \infty , \qquad (2)$$

where $\hat{\psi}(\omega)$ is the Fourier transform of $\psi(t)$ at frequency ω.

If a signal $f(t)$ is deconstructed into the function set, the continuous wavelet transform $(W_\psi f)$ is defined as

$$(W_\psi f)(a,b) = <f, \psi_{a,b}> = |a|^{1/2} \int_{-\infty}^{\infty} f(t)\bar{\psi}\left(\frac{t-b}{a}\right) dt , \qquad (3)$$

where "$< >$" indicates the inner product; $(W_\psi f)(a,b)$ are the coefficients of wavelet transform corresponding to scale and location (a and b); $\bar{\psi}$ represents the conjugations of ψ; This transform is known as a continuous wavelet transform (CWT) when a and b are continuously changing, and as a discrete wavelet transform (DWT) when a and b are discrete points.

Typically, a and b are taken as power series:

$$a = a_0^j ; \quad b = k a_0^j b_0 ; \quad j, k \in Z . \qquad (4)$$

When $a_0 = 2$ and $b_0 = 1$, the scale and translation are dyadic discrete and the dyadic wavelet is obtained:

$$\psi_{j,k}(t) = 2^{j/2} \psi(2^{-j}t - k) . \qquad (5)$$

Hereafter, the DWT is represented as this dyadic wavelet transform, and the DWT coefficients are

$$c_{j,k} = \int_{-\infty}^{\infty} f(t)\bar{\psi}_{j,k} dt . \qquad (6)$$

$c_{j,k}$ is the kth largest value of the coefficients in the jth deconstruction level;

The reconstruction formula is

$$f(t) = \sum_{j \in Z} \sum_{k \in Z} c_{j,k} \psi_{j,k}(t) . \qquad (7)$$

Different wavelet functions have different characteristics: (1) Compact support, which denotes the attenuation of the generating wavelet; the narrower the width of the support, the faster the attenuation, and the better the localization. (2) Orthogonality, which indicates the continuously differentiable number and the smoothness of the wavelet function; the better the orthogonality, the faster the convergence. (3) Symmetry, which relates to whether the wavelet filtering is in a linear phase that closely connects with the signal distortion after reconstruction. (4) Vanishing moments, which can be physically regarded as a convergence rate when the wavelet function approaches a signal, i.e., when a signal is transformed by the wavelet, the wavelet is required to have compact support or acute attenuation in both the time and frequency domains; the higher the order of vanishing moments, the better the smoothness, and the stronger the ability to mirror the high-frequency details. (5) Regularity, which is related to smoothness of a signal; the greater the regularity index, the smoother the signal, and the localization characteristics can be estimated according to the regularity index at each point in a signal.

However, such a generating wavelet function, which not only has compact support and symmetry but also has good orthogonality and vanishing moments, does not exist. The shorter the support width, the poorer the smoothness, so the compact support and the smoothness are two contradictory aspects. In addition, except for the Haar wavelet, which can meet the orthogonal and symmetric conditions at the same time but has poor localization performance, such a wavelet with both orthogonality and symmetry does not exist either, so orthogonality and symmetry are also contradictory.

2.2. Threshold strategies

(1) Penalty threshold strategy (Yang, 2007):

Given that t^* is the positive integer that makes function $f(t)$ minimum:

$$f(t) = -\sum_{k \leqslant t} c_{j,k}^2 + 2\sigma^2 t[\alpha + \log(m/t)] , \qquad (8)$$

where variable $t \in [1, m]$; σ is the noise intensity of the signal; α is an experience value, which is a real number greater than one; and m is the total number of coefficients; then the threshold value T corresponding to the value t^* is:

$$T = |c_{j,t^*}| . \qquad (9)$$

To avoid the impact of a boundary effect on the wavelet coefficient calculation, the estimation of the standard deviation of noise level is calculated by the absolute value of the detail coefficients. When the signal is regular enough, the details of the signal are concentrated into the minority of the coefficients, so the penalty threshold is a suitable threshold strategy.

(2) Φ_{DP} penalty threshold strategy:

The largest deviation value of Φ_{DP} in each deconstruction level can be estimated according to the scope of the polarmetric parameter in raindrop echoes, so the wavelet detail coefficients larger than the deviation can be considered as non-weather echoes, such as clutters, δ, or other noises, which need to be filtered out. For C-band radar, K_{DP} is generally not larger than $6° \ \mathrm{km}^{-1}$, taking into account fluctuation, and the detail coefficients in the first level will not exceed $8 \times 0.3 = 2.4 \ (°)$, where $2^1 \times 0.15 = 0.3 \ \mathrm{(km)}$ is the resolution in the first level. Because the size of the time-frequency window is constant to the wavelet function, the detail coefficients over $2.4°$ can be considered as noise in each level, and the Φ_{DP} penalty threshold strategy is defined as:

$$T = 2.4 . \qquad (10)$$

(3) Default threshold strategy:

This is given by the formula

$$T = \sqrt{2\log(n)} \times \sigma , \qquad (11)$$

where n is the length of the discrete signal.

2.3. *Threshold functions*

After the detail coefficients are suppressed by a certain threshold strategy, a threshold function is needed to reconstruct the signal. Hard and soft threshold functions (Donoho, 1995) are commonly used:

Hard threshold function:

$$\hat{c}_{j,k} = \begin{cases} c_{j,k} , & |c_{j,k}| \geqslant T , \\ 0 , & |c_{j,k}| < T ; \end{cases} \tag{12}$$

Soft threshold function:

$$\hat{c}_{j,k} = \begin{cases} \mathrm{sgn}(c_{j,k})(|c_{j,k}| - T) , & |c_{j,k}| \geqslant T , \\ 0 , & |c_{j,k}| < T , \end{cases} \tag{13}$$

where $\hat{c}_{j,k}$ are the coefficients after processing and sgn( ) is the sign function.

3. The de-noising steps by wavelet analysis

3.1. *Construct a simulation signal*

To illustrate the performance of wavelet function de-noising, two neighboring precipitation cells are simulated with the gamma drop size distribution (DSD) (Ulbrich, 1983, Chandrasekar et al., 1990, Scarchilli et al., 1993)

$$N(D) = N_0 D^{\mu} e^{-(3.67+\mu)D/D_0} , \tag{14}$$

where N is the raindrops number per unit volume per unit size interval; D is the equivalent volume diameter of raindrops (mm); N_0 is the concentration parameter that is assumed to have the value of 8×10^3 mm^{-1} m^{-3}; μ is the distribution parameter and is assumed to be zero; and D_0 is the median volume diameter, and is assumed to be

$$D_0(r) = D_{\max} e^{\left[-2\ln 2 \left(\frac{r - r_{\max}/2}{r_{\max}}\right)^2\right]} , \tag{15}$$

where $D_{\max}$ is the maximum equivalent diameter of raindrops and is assumed to be 0.2 cm; $r_{\max}$ represents the diameters of cells, with the first one assumed to be 30 km and the next 15 km; and r is the distance between a raindrop to each cell center.

Assume that the radar wavelength is 5.6 cm, and the gate width is 150 m, so the beam passes through the simulation rain area with 300 gates. The particle scattering is calculated using the method of extended boundary conditions with the

consideration of the relationship between the drop size and the ellipticity (Liu et al., 1989), and the range profiles of the horizontal reflectivity factor Z_H and Φ_{DP} are shown in Fig. 1 (the radar is located at 0 km).

3.2. *Mixed signal noise*

Because radar does not measure Φ_{DP} directly, the total differential phase Ψ_{DP} is estimated from the co-polar covariance that consists of both forward propagation and backscattering phase shifts, δ:

$$\Psi_{DP}(r) = \Phi_{DP}(r) + \delta(r) , \tag{16}$$

Generally, ground clutters can cause severe change in Φ_{DP} over a very short distance, and large oblate raindrops and melting hailstones can cause δ, which will increase the phase shifts from several degrees to about 30° for C-band radar. To simulate real situations, some phase shifts are intentionally increased into the Φ_{DP} simulation signal in Fig. 1b, from 46 to 55 gates simulating clutters, from 96 to 105 gates simulating a long-distance δ (hereafter referred to as δ_l), and from 249 to 252 gates simulating a short-distance δ (hereafter referred to as δ_s). Simulating the short- and long-distance δ is for contrasting the de-noising effect to different scales of noises by wavelet multiscale analysis. The added phase shift values (units: °) are listed in Table 1. For convenience, the no-noise Φ_{DP} signal in Fig. 1b is hereafter represented by s; s polluted by clutters and δ is represented by s_p; and s_p further mixed by 15 dB SNR white noise is represented by s_n. In actual radar observations, when the SNR is too small, the
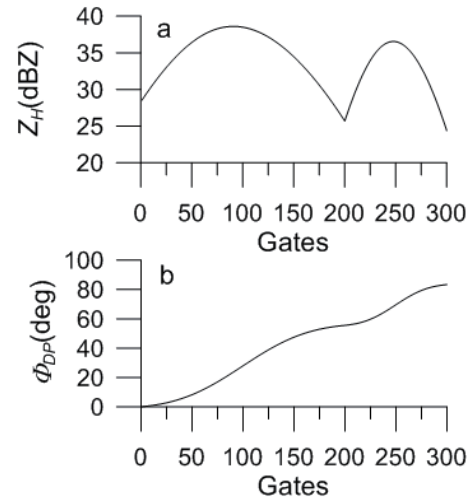

Fig. 1. Images of the simulation results: (a) Z_H and (b) Φ_{DP} range profile.

Table 1. The added phase shift values (°) by clutters and δ at some gates in s to simulate an actual noisy signal.

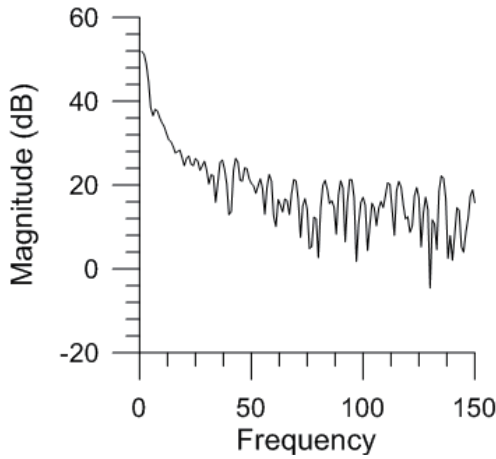| Terms					Values					
Gates	46	47	48	49	50	51	52	53	54	55
Clutters (°)	−30	30	60	−60	30	−60	30	−30	−50	50
Gates	96	97	98	99	100	101	102	103	104	105
Long δ (°)	10	10	15	10	20	30	15	30	15	10
Gates	249	250	251	252						
Short δ (°)	10	20	30	15						

Fig. 2. Frequency distribution of s_n.

weak signals have no value because two receivers have difficulty ensuring their consistency (Hu et al., 2012).

Figure 2 shows the results of the Fourier analysis of s_n. As shown in Fig. 2, when the frequency is greater than 15, i.e., the distance is less than 3.0 km ($300/15 \times 150$ m), the magnitude of the Fourier coefficients is less than 30 dB, so these high-frequency variations can be considered as noises that need to be suppressed, and then the signal is reconstructed by inverse Fourier transform. However, this method is too drastic because a large amount of useful information is inhibited and many energy components in the original signal are lost.

3.3. *Deconstruct and analyze the wavelet coefficients*

Without loss of generality, s_n is deconstructed into five levels with the db5 wavelet, and the approximation and detail coefficients in each level are shown in Fig. 3, wherein Figs. 3a and g are s_p and s_n, respectively; Figs. 3b–f are the approximation coefficients represented by a_1 to a_5, respectively; and Figs. 3h–l are the detail coefficients represented by d_1 to d_5 from levels 1–5, respectively.

First, let us analyze the behavior of the approximation coefficients that represent the low-frequency change. The location of clutters and two δ are seen in the first- and second-level approximation coefficients, a_1 and a_2. The two δ are obvious, and clutters can be vaguely identified in a_3. The two δ still have weak responses, but clutter almost disappears in a_4. The spatial scale in the fifth level is $2^5 = 32$ gates; that is, 4.8 km, so a_5 is smooth enough to approximate s.

Continuing to analyze the detail coefficients that represent the high frequency change, to highlight the changes, note that the scale of the y-axis in each level is different. Because the clutters are high-frequency changes, the energy of clutters is much larger than that of other noise, so the location of clutters can be observed very clearly in the first-level detail coefficient, d_1, but the two δ, which are drowned in noise, cannot be observed. The amplitude of the detail coefficients d_2 and d_3 are reduced in the second and third levels, wherein the clutter feature can still be identified, and the position of δ_s begins to emerge slightly, but the δ_l does not appear as its

lower frequency characteristic. The amplitude of d_4 and d_5 is further decreased, the position of δ_l emerges obviously, and the clutter and δ_s can be recognized roughly in d_4. The detail coefficient d_5 reflects the fluctuations of the low-frequency signal in which the two δ can vaguely be identified, but the clutter disappears completely.

By the above demonstration, the different types and scale noises can be separated into each deconstruction level easily for their different frequency characteristics, and conveniently further processed.

3.4. *The process of wavelet de-noising*

As mentioned above, the basic noise model can be expressed as

$$s_n(n) = s(n) + \sigma e(n) \,, \tag{17}$$

where $e(n)$ is the noise; σ is the noise intensity that is generally determined by the standard deviation of coefficients in each deconstruction level; and n is the length of the discrete signal. The goal of wavelet de-noising is to suppress $e(n)$ and restore $s(n)$. The steps of wavelet de-noising are generally performed as below:

(1) Deconstruction: a signal is deconstructed into N levels with a selected wavelet function.

(2) De-noising: the detail coefficients in each level are suppressed with a selected threshold strategy.

(3) Reconstruction: the signal is reconstructed by means of the approximation and the processed detail coefficients with a selected threshold function.

According to the above discussion without loss of generality, hereafter the db5 wavelet function is used to deconstruct a signal into five levels, and two de-noising schemes are designed: (1) suppression by the penalty threshold strategy and reconstruction by the soft threshold function scheme (PSS); (2) Φ_{DP} penalty strategy and soft function scheme (PPSS).

4. Analysis of two cases

A mobile C-band dual polarimetric weather radar (POLC), which transmits and receives the horizontal and

Table 2. Main characteristics of POLC radar.

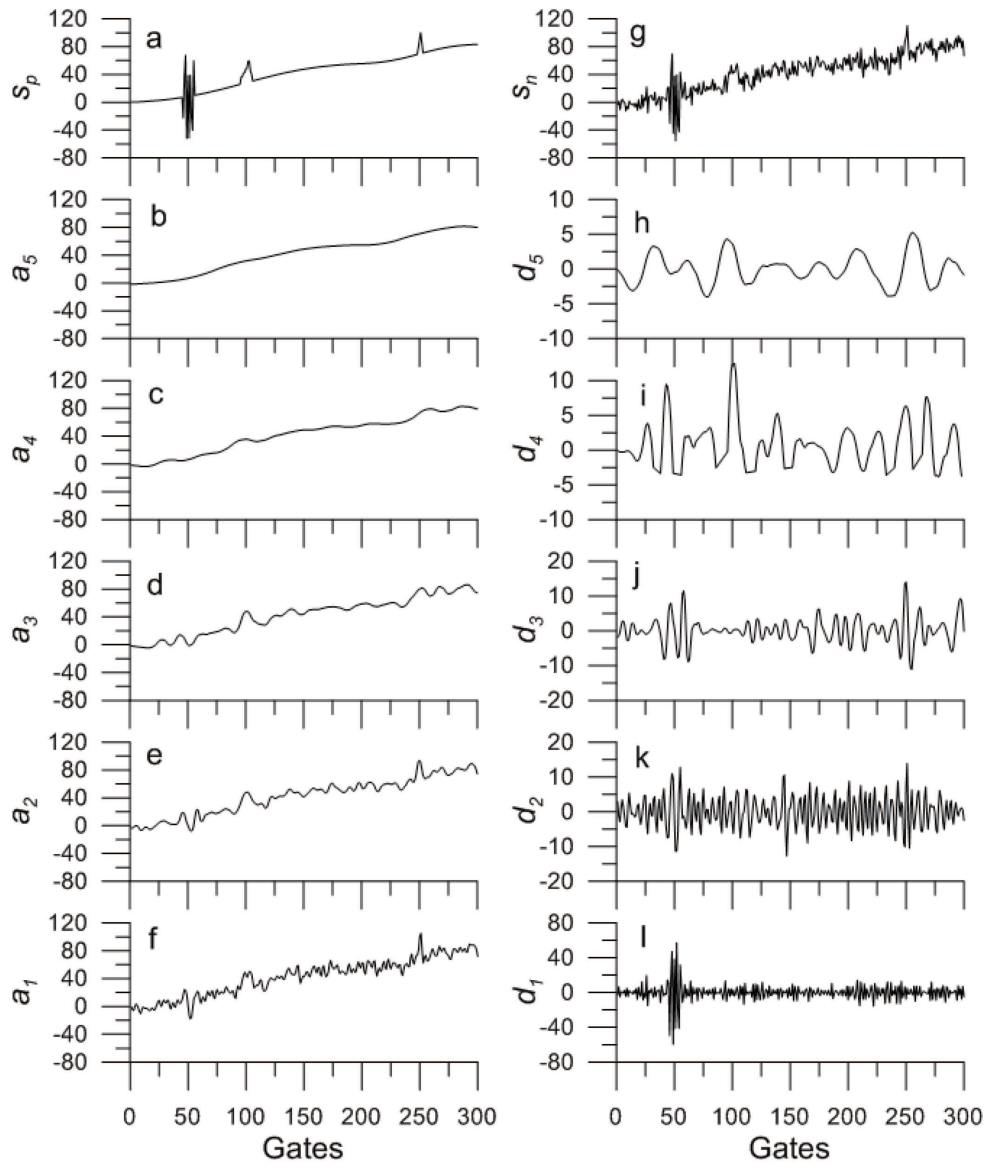| Parameters	Values
Antenna Diameter	3.2 m
Gain	40 dB
Beam width	1.2°
First side lobe	< -25 dB
Isolation	> 40 dB
Wavelength	5.5 cm
Pulse width	1.0/0.5 μs
Peak power	$\geqslant 250$ kw
PRF	300–1200 Hz
Polarization	Horizontal and vertical
Minimum detectable signal	$\leqslant -109$ dBm
Receiver noise figure	$\leqslant 3.0$ dB
Receiver Dynamic range	> 85 dB
Observation range	150 km

Fig. 3. The result of s_n deconstructed into five levels with the db5 wavelet: (a) s_p; (b–f) approximation coefficients from a_1 to a_5; (g) s_n; (h–l) detail coefficients from d_1 to d_5.

vertical polarization signals simultaneously, was first developed in China in 2008. The radar operated at a frequency of 5.43 GHz and a 150-m gate width (Hu et al., 2012), and the main characteristics of the radar are summarized in Table 2. The following two representative actual cases are selected to examine the effects of noise reduction by the methods described above. Because the height of the antenna is only about 6.5 m, it is blocked by surroundings that cause some missing beams in the PPIs.

4.1. *Squall line case*

A squall line was detected by POLC radar in the afternoon of 17 July 2008 in Shouxian, Anhui Province. A total of 200 gates (30 km) from 40 to 239 were analyzed in the Φ_{DP} radial data in the elevation of $1.5°$ and azimuth of $200°$ at 1828 LST. The radial profile of Z_H along with the gates is

shown in Fig. 4.

The Ψ_{DP} values (Fig. 5a) from gates 86 to 89 are $-119.5, -106.58, -102.22$ and -121.33, respectively. It is shown that the values in gates 87 and 89 exhibited jumps of $13°$ and $19°$ due to backscattering δ and that the values from gates 105 to 108 exhibited jumps of over $20°$. The section of the Ψ_{DP} signal is deconstructed into five levels with the db5 wavelet, and then the detail coefficients are suppressed by the Φ_{DP} penalty threshold. The detail coefficients before and after suppression are shown in Fig. 5, where the images of approximation coefficients are not shown.

Figure 6 shows the de-noising results of the Ψ_{DP} section using the PPSS, Kalman, mean (15 points), median (15 points) and FIR (once) filters. All these filters can de-noise to a certain extent, but the Kalman filter has a larger signal distortion, and the median is rougher than the others. Because
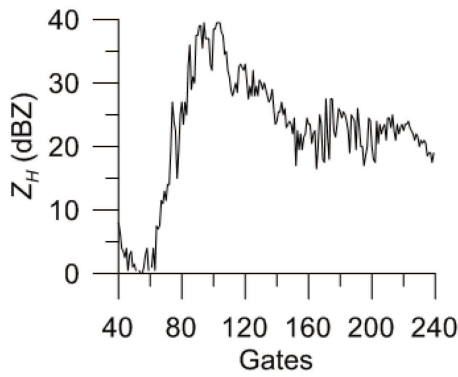
Fig. 4. The range profile of Z_H from gates 40–239 (slope distance of 6–36 km) at elevation 1.5° and azimuth 200° at 1828 LST on 17 July 2008.

the color-key resolution of Φ_{DP} is about 30°, it is hard to show the differences among these methods, but K_{DP}, obtained with 13-gate fitting, is selected to illustrate the differences (Figs. 7a–f). Figure 7 shows part of the PPI images of the squall case at the same time and elevation angle as in Fig. 4, in

which the de-noising methods of Figs. 7a–f correspond to Fig. 6, Figs. 7g and h are the raw Z_H and Φ_{DP}, respectively, and the interval of the range ring is 15 km. From Fig. 7h, the Φ_{DP} increases rapidly in the south-southwest. All the de-noised pictures (Figs. 7b–f) are smoother than the raw image (Fig. 7a). Focusing on the area between azimuth 240° and 270° and the range between 15 and 30 km, the PPSS (Fig. 7b), mean (Fig. 7d), and median (Fig. 7e) methods can preserve more details. In other words, using these methods it is still easy to determine the center of the heavy rainfall after de-noising. The Kalman filter (Fig. 7c) method is smoother than the others, but lost more details. The FIR approach has a more obvious boundary effect (Fig. 7f), which can cause great errors at the edges of rain clouds.

4.2.   *Typhoon Koppu case*

The landing typhoon Koppu was observed by POLC radar from 14 to 15 September 2009 in Zhuhai, Guangdong Province, and it caused serious backscatter phase shift δ because of carrying lots of large raindrops on Φ_{DP} measurements. The beam at elevation 1.5° and azimuth 237° at 0443 LST passed through hills ranging from 15 to 25 km,
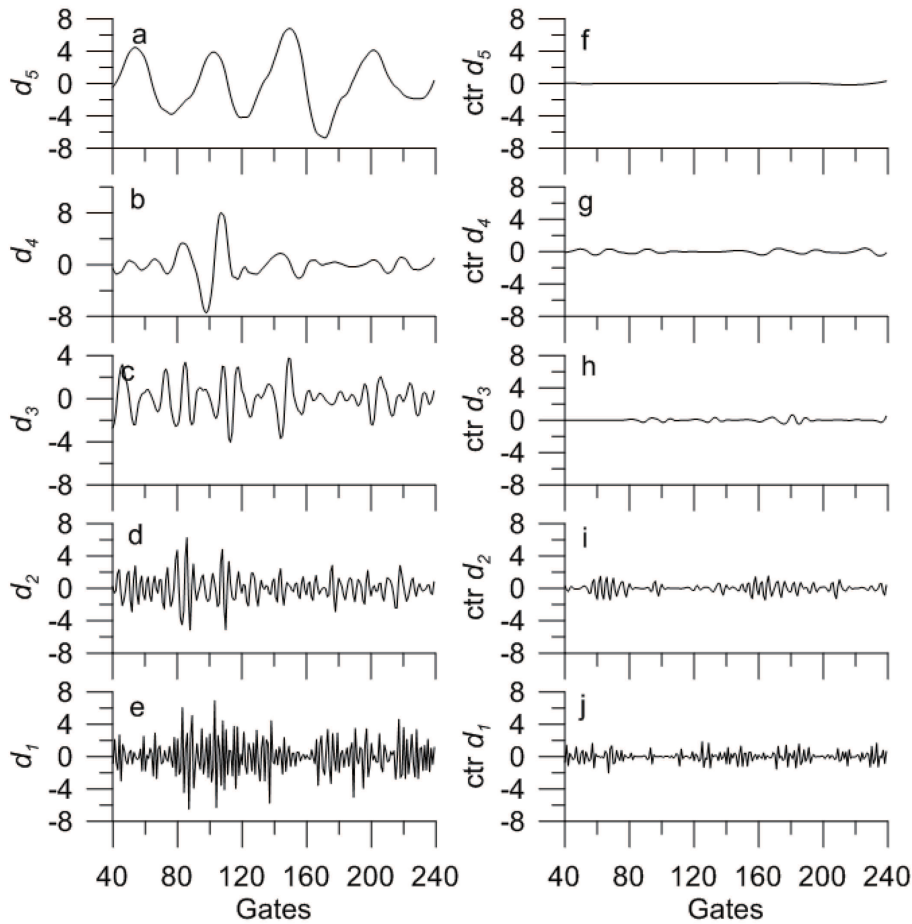

Fig. 5. The section of the Ψ_{DP} signal in Fig. 6a is deconstructed into five levels with the db5 wavelet, and then the detail coefficients in each level are suppressed by the Φ_{DP} penalty threshold. The left-hand panels (a–e) are the details without suppression, and the right-hand panels (f–j) are after suppression.
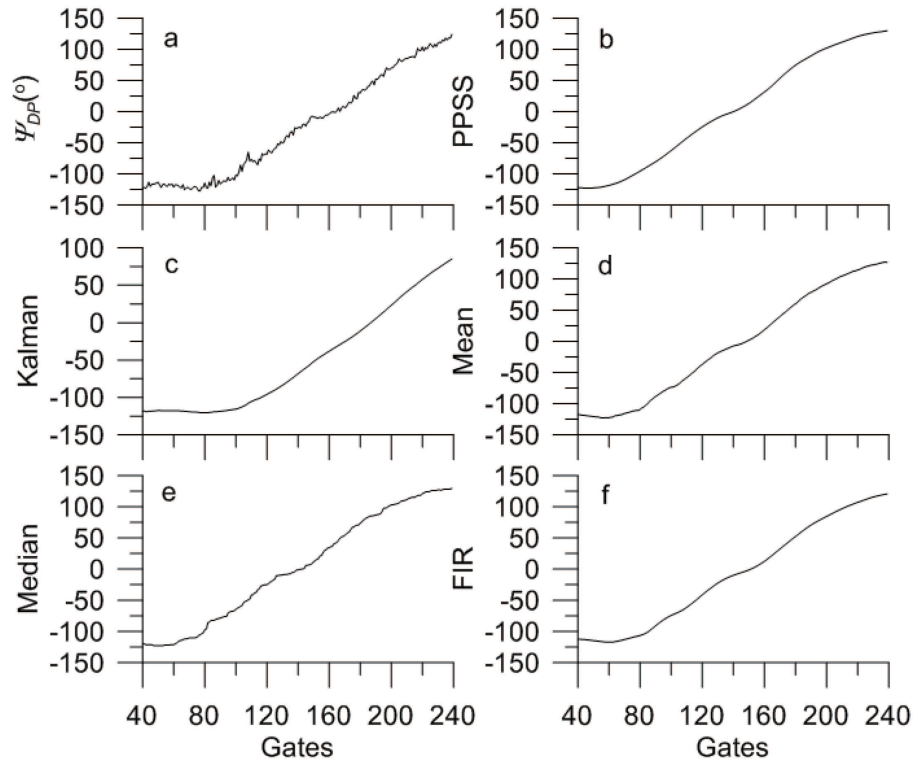
Fig. 6. The (a) Ψ_{DP} section corresponding to Fig. 4 and de-noised by the (b) PPSS, (c) Kalman, (d) mean, (e) median, and (f) FIR filters, respectively.
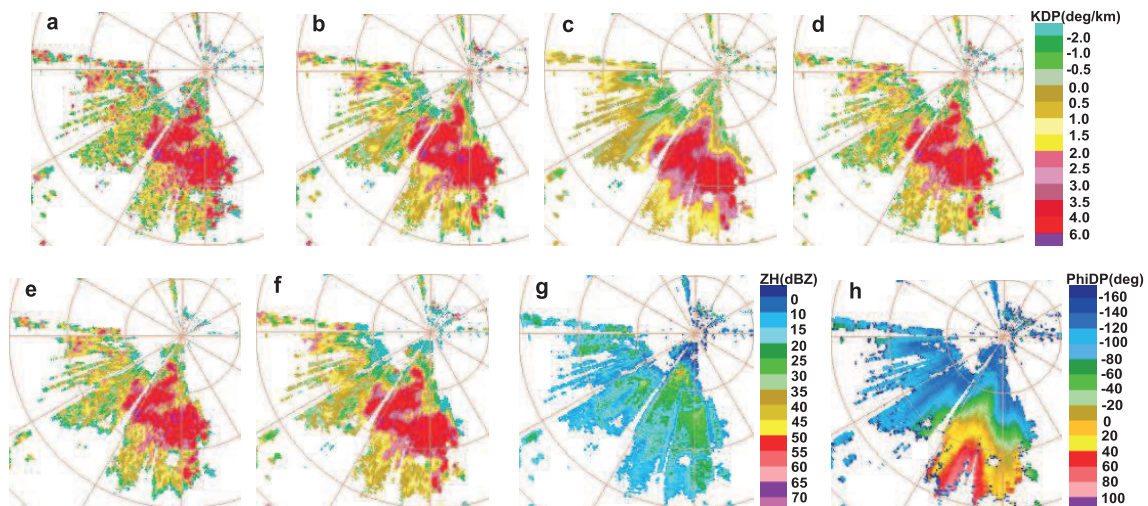

Fig. 7. Part of the K_{DP} PPI images of the squall case at the same time and elevation angle as in Fig. 4. The de-noising methods of Figs. 7a–f corresponding to Figs. 6, 7g and h show the raw Z_H and Φ_{DP}, respectively, in which the interval of the range ring is 15 km.

and through a heavy precipitation area from about 75 to 100 km behind the typhoon eye. Therefore, its Φ_{DP} data are a good example to illustrate the mitigation of multiscale mixed noises. Since the maximum continuous contaminated Φ_{DP} distance can be more than 5 km in such a violent typhoon, the Φ_{DP} data are deconstructed into six levels with the wavelet function db5; namely, the maximum distinguishable noise scale is $2^6/2 \times 0.15$ km $= 4.8$ km. The mean and median

filters are performed with 31 points (31×0.15 km $= 4.65$ km). The pictures of wavelet deconstruction coefficients are not shown. The radial profiles of raw Z_H, Ψ_{DP}, and Ψ_{DP} after de-noising by the above methods are shown in Fig. 8, and their corresponding PPIs are shown in Fig. 9, in which the interval of the range ring is 30 km.

As can be seen from Figs. 8a and b, the data of Z_H and Ψ_{DP} fluctuate drastically around the 100th gate for the ground
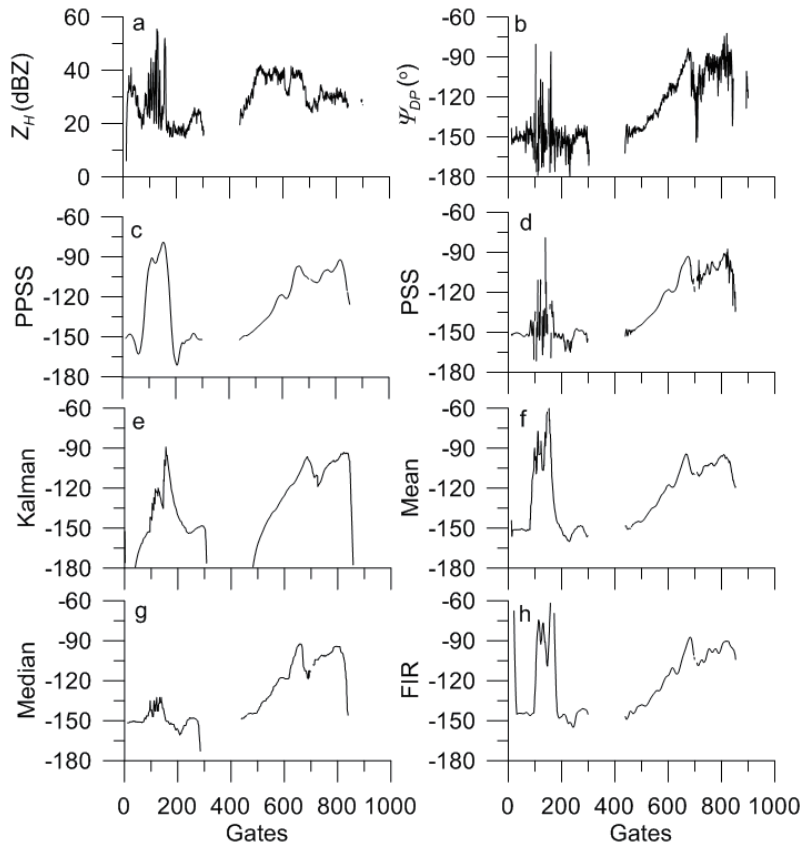
Fig. 8. The range profiles of raw (a) Z_H, (b) Ψ_{DP}, and Ψ_{DP} after de-noising by the (c) PPSS, (d) PSS, (e) Kalman, (f) mean, (g) median, and (h) FIR filters at elevation 1.5° and azimuth 237° at 0443 LST 15 September 2009.
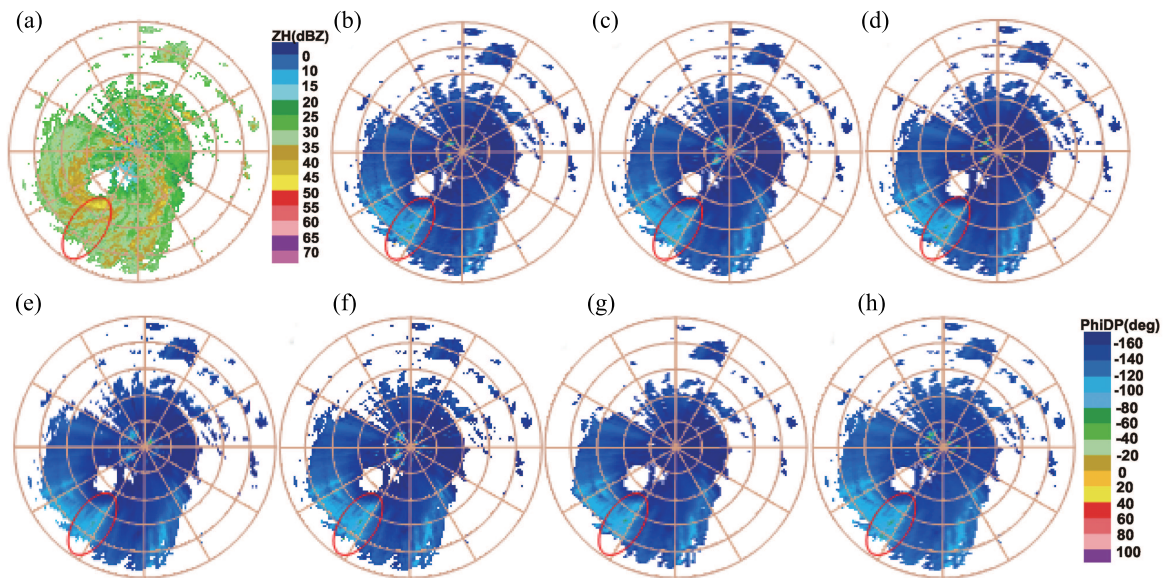

Fig. 9. The PPI images corresponding to Fig. 8, in which the interval of the range ring is 30 km, and mainly focusing on the area enclosed with red ellipses in (b–h).

clutter. In the area between the 500th and 700th gates, approximately, the Ψ_{DP} data have several peaks that influence

gates 5–30 by δ, and the measured Z_H reaches about 40 with the maximum value of 42 dBZ. The SNRs are smaller than 20

dB behind the 700th gate, so the data quality becomes poor and will not be discussed here. Figures 8c–h are the radial profiles of Ψ_{DP} de-noising by the PPSS, PSS, Kalman, mean, median, and FIR methods, respectively. It can be seen that the PSS method retains the largest amount of clutter information for further identification. Both PSS and PPSS de-noise well, especially in the hybrid noise area behind the typhoon eye, and this means that more effective K_{DP} data can be obtained. As in Fig. 6, the Kalman filter has larger distortion, and the others have a few remains of pollution.

From Fig. 9, all the methods perform well, and at first sight it seems there is no difference between these pictures because the color-scale interval is too large to the change value after de-nosing. However, when we focus on the area enclosed by red ellipses in images of Φ_{DP} (Figs. 9b–h) , the features of color distribution and gradation in Figs. 9c and d (PPSS and PSS) are more similar to Fig. 9b (raw Φ_{DP}) than the other figures, which suggests that wavelets have less distortion. In particular, the clutters are almost coincident between Figs. 9b and d, which fully demonstrates the stronger ability of retaining details by the PSS method compared to the other ones. This is useful for further processing in some dual radar algorithms, such as quantitative precipitation estimation, to avoid the contamination of clutters and the location of heavy rainfall.

5. Summary and discussion

As polarimetric parameters are easily affected by noise effective applications of polarization radar have been limited for many years and noise mitigation methods have been introduced since the invention of polarization radar. This paper introduces a wavelet multiscale analysis method, which has been widely used in many other fields. Using simulations and actual Φ_{DP} data as examples, the processes and results of wavelet de-noising are presented in detail and, further, a Φ_{DP} penalty threshold strategy is proposed according to the characteristics of the polarimetric parameter.

Owing to multiscale analysis, and depending on the purpose of de-noising, wavelet analysis can not only smooth a signal very well, but can also retain enough detail to accurately indicate the clutters and strong echoes, even if they have a small amount of energy in the frequency domain.

According to the characteristics of precipitation echoes, the deconstruction scales typically do not overrun more than five levels, which have a satisfactory de-noising effect, and avoid causing extra errors when small-scale noises are deconstructed into a large number of levels.

The noise reduction can be obviously influenced by the selection of threshold strategies and functions. As described in this paper, the Φ_{DP} penalty is a very effective strategy for Φ_{DP} data de-noising, which can retain more details after being combined with the hard-threshold function, but a smoother signal with the soft one.

In this paper we have attempted to introduce the wavelet analysis approach in polarimetric radar data quality control, and the results are encouraging. With the swift development of computing technology, a volume span data can be processed within one minute by wavelet analysis with a personal computer. Therefore, further work could be carried out in the future to select, or even construct, a particular wavelet generating function, and design a pertinent threshold strategy and function for better de-noising performance for each polarimetric parameter.

APPENDIX

The Coefficients of the FIR Method and Process of the Kalman Filter

The coefficients of the FIR are shown in Table A1, wherein the 20th-order filter is symmetric, and the coefficients are shown for the complex variable Z (Proakis and Manolakis, 1988). The magnitude of the response of the FIR filter is shown in Fig. A1.

Table A1. FIR filter coefficients.

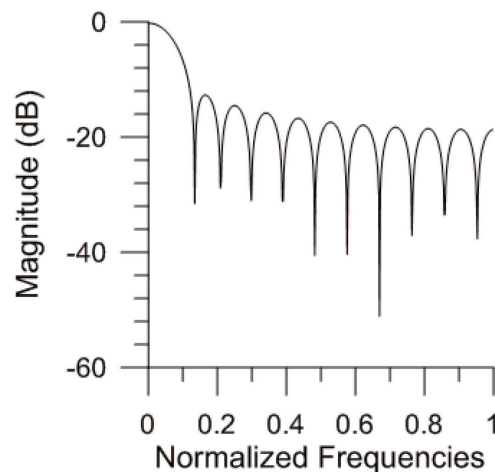| Z order	Coefficient	Z order
Z^0	$1.625807356 \times 10^{-2}$	Z^{-20}
Z^{-1}	$2.230852545 \times 10^{-2}$	Z^{-19}
Z^{-2}	$2.896372364 \times 10^{-2}$	Z^{-18}
Z^{-3}	$3.595993808 \times 10^{-2}$	Z^{-17}
Z^{-4}	$4.298744446 \times 10^{-2}$	Z^{-16}
Z^{-5}	$4.971005447 \times 10^{-2}$	Z^{-15}
Z^{-6}	$5.578764970 \times 10^{-2}$	Z^{-14}
Z^{-7}	$6.089991897 \times 10^{-2}$	Z^{-13}
Z^{-8}	$6.476934523 \times 10^{-2}$	Z^{-12}
Z^{-9}	$6.718151185 \times 10^{-2}$	Z^{-11}
Z^{-10}	$6.800100000 \times 10^{-2}$	

Fig. A1. Magnitude of the response of the FIR filter used in the de-noising.

Table A2. Meaning of each term in Eq. (A1)–(A6).

Letter	Meaning
$X(r)$	System state
$Z(r)$	Measured value
r	At the distance r
A	System matrix
B	State transition matrix
C	Measured matrix
$d(r)$	Process noise, Gaussian Distribution with zero mean and Q variance, i.e. $p(d) \sim N(0,Q)$
$V(r)$	Measurement noise, Gaussian Distribution with zero mean and R variance, i.e. $p(V) \sim N(0,R)$

For Φ_{DP}, the process and measurement equations of the Kalman filter are:

$$X(r) = AX(r-1) + Bd(r-1), \tag{A1}$$

$$Z(r) = CX(r) + V(r), \tag{A2}$$

$$X(r) = \begin{bmatrix} \Phi_{DP}(r) \\ K_{DP}(r) \end{bmatrix}, \tag{A3}$$

$$A = \begin{bmatrix} 1 & r \\ 0 & r \end{bmatrix}, \tag{A4}$$

$$B = \begin{bmatrix} r^2/2 \\ r \end{bmatrix}, \tag{A5}$$

$$C = \begin{bmatrix} 1 & 0 \end{bmatrix}, \tag{A6}$$

where the meanings of each term in Eqs. (A1)–(A6) are listed in Table A2 (He et al., 2009).

REFERENCES

Aydin, K., V. N. Bringi, and L. Liu, 1995: Rain-rate estimation in the presence of hail using S-band specific differential phase and other radar parameters. *J. Appl. Meteor.*, **34**, 404–410.

Bringi, V. N., and V. Chandrasekar, 2001: *Polarimetric Doppler Weather Radar: Principles and Applications.* Cambridge University Press, 662 pp.

Chandrasekar, V., N. Balakrishnan, and D. S. Zrnić 1990: Error structure of multi-parameter radar and surface measurements of rainfall, Part III: Specific differential phase. *J. Atmos. Oceanic Technol.*, **7**, 621–629.

Chandrasekar, V., V. N. Bringi, S. A. Rutledge, A. Hou, E. Smith, G. S. Jackson, E. Gorgucci, and W. A. Petersen, 2008: Potential role of dual-polarization radar in the validation of satellite precipitation measurements: Rationale and opportunities. *Bull. Amer. Meteor. Soc.*, **89**, 1127–1145, doi: 10.1175/2008 BAMS2177.1.

Daubechies, I., 1988: Orthonormal bases of compactly supported wavelets. *Commun. Pure Appl. Math.*, **41**, 909–996.

Desrochers, P. R., and S. Y. K. Yee, 1999: Wavelet applications for mesocyclone identification in Doppler radar observations. *J. Appl. Meteor.*, **38**, 965–980.

Donoho, D. L., 1995: De-noising by soft-thresholding. *IEEE Trans. Inform. Theory*, **41**, 613–627.

Grossmann, A., and J. Morlet, 1984: Decomposition of Hardy Functions into Square Integrable Wavelets of Constant Shape. *SIAM J. Math. Anal.*, **15**(4), 723–736.

He, Y. X., D. R. Lü, and H. Xiao, 2009: Attenuation correction of reflectivity for X-band dual polarization radar. *Chinese J. Atmos. Sci.*, **33**(5), 1027–1037. (in Chinese)

Hu, Z. Q., L. P. Liu, and L. R. Wang, 2012: A quality assurance procedure and evaluation of rainfall estimates for C-band polarimetric radar. *Adv. Atmos. Sci.*, **29**(1), 144–156, doi: 10.1007/s00376-011-0172-y.

Hubbert, J., and V. N. Bringi, 1995: An iterative filtering technique for the analysis of copolar differential phase and dual-frequency radar measurements. *J. Atmos. Oceanic Technol.*, **12**, 643–648.

Hubbert, J., V. Chandrasekar, V. N. Bringi, and P. Meischner, 1993: Processing and interpretation of coherent dual-polarized radar measurements. *J. Atmos. Oceanic Technol.*, **10**, 155–164.

Jameson, A. R., 1985: Microphysical interpretation of multiparameter radar measurements in rain. Part III: Interpretation and measurement of propagation differential phase shift between orthogonal linear polarizations. *J. Atmos. Sci.*, **42**, 607–614.

Jordan, J. R., R. J. Lataitis, and D. A. Carter, 1997: Removing ground clutters and intermittent clutters contamination from wind profiler signal using wavelet transforms. *J. Atmos. Oceanic Technol.*, **14**, 1280–1297.

Liu, L. P., B. X. Xu, and Q. M. Cai, 1989: The effects of attenuation by precipitation and sampling error on measuring accuracy of 713 type dual linear polarization radar. *Plateau Meteorology*, **8**(2), 181–188. (in Chinese)

Liu, S., M. Xue, and Q. Xu, 2007: Using wavelet analysis to detect tornadoes from Doppler radar radial-velocity observations. *J. Atmos. Oceanic Technol.*, **24**, 344–359, doi: 10.1175/ JTECH1989.1.

Mallat, S., 1989: A theory for multi-resolution signal decomposition: The wavelet representation. *IEEE Transactions on Pattern Analysis and Machine Intelligence*, **11**(7), 674–693.

Mallat, S., and W. L. Hwang, 1992: Singularity detection and processing with wavelets. *IEEE Transactions on Information Theory*, **38**(2), 617–643.

Meyer, Y., 1993: *Wavelets: Algorithms and Applications.* Society for Industrial and Applied Mathematics, Philadelphia, PA, 133 pp.

Proakis, J. G., and D. G. Manolakis, 1988: *Introduction to Digital Signal Processing.* Macmillan Publishing Co., 944 pp.

Scarchilli, G., E. Gorgucci, V. Chandrasekar, and T. A. Seliga, 1993: Rainfall estimation using polarimetric technique at C-band frequencies. *J. Appl. Meteor.*, **32**, 1150–1160.

Seliga, T. A., and V. N. Bringi, 1978: Differential reflectivity and differential phase shift: Applications in radar meteorology. *Radio Sci.*, **13**, 271–275.

Ulbrich, C. W., 1983: Natural Variations in the analytical form of the raindrop size distribution. *J. Appl. Meteor.*, **22**, 1764–1775.

Wang, Y. T., and V. Chandrasekar, 2009: Algorithm for estimation of the specific differential phase. *J. Atmos. Oceanic Technol.*, **26**, 2565–2578, doi: 10.1175/2009JTECHA1358.1.

Xu, Y., J. B. Weaver, D. M. Healy Jr., and J. Lu, 1994: Wavelet transform domain filters: A spatially selective noise filtration technique. *IEEE Transactions on Image Processing*, **3**(6), 747–758.

Yang, J. G., 2007: *Wavelet Analysis and Its Engineering Applications.* China Machine Press, 187 pp. (in Chinese)

Zhang, P. C., B. Y. Du, and Dai, T. P., 2001: *Radar Meteorology.* China Meteorological Press, 260–266.

Zrnić D. S., and A. Ryzhkov, 1996: Advantages of rain measurements using specific differential phase. *J. Atmos. Oceanic Technol.*, **13**, 454–464.